

**Design Principles of Pseudocapacitive Carbon Anode
Materials for Ultrafast Sodium and Potassium-ion Batteries**

Journal:	<i>Journal of Materials Chemistry A</i>
Manuscript ID	TA-ART-02-2020-001821.R1
Article Type:	Paper
Date Submitted by the Author:	14-Mar-2020
Complete List of Authors:	Gao, Yong; Northwestern Polytechnical University Xi'an, CN Zhang, Jing; Northwestern Polytechnical University Li, Nan; Northwestern Polytechnical University Han, Xiao; Northwestern Polytechnical University, School of materials science and engineering Luo, Xian; Northwestern Polytechnical University, Department of Applied Chemistry Xie, Keyu; Northwestern Polytechnical University Wei, Bingqing; University of Delaware, Mechanical Engineering Xia, Zhenhai; University of North Texas, Department of Materials Science and Engineering

ARTICLE

Design Principles of Pseudocapacitive Carbon Anode Materials for Ultrafast Sodium and Potassium-ion Batteries

Yong Gao^a, Jing Zhang^a, Nan Li^a, Xiao Han^a, Xian Luo^a, Keyu Xie^a, Bingqing Wei^b, and Zhenhai Xia^{*c}

Sodium- and potassium-ion batteries are one of the most promising electrical energy storage devices at low cost, but their inferior rate and capacity have hampered broader applications such as electric vehicles and grids. Carbon nanomaterials have been demonstrated to have ultrafast surface-dominated ion uptake to drastically increase the rate and capacity, but trial-and-error approaches are usually used to find desired anode materials from numerous candidates. Here, we developed guiding principles to rationally screen pseudocapacitive anode from numerous candidate carbon materials to create ultrafast Na and K-ion batteries. The transition from pseudocapacitive to metal-batteries mechanisms on heteroatom-doped graphene in the charging process was uncovered by the density functional theory methods. The results show that graphene substrate can guide the preferential growth of K and Na along graphene plane, which inhibits dendrite development effectively in the batteries. An intrinsic descriptor is discovered to establish a volcano-shaped relationship that correlates the capacity with the intrinsic physical qualities of the doping structures, from which the best anode materials could be predicted and synthesized. The predictions are in good agreement with the experimental results. The strategies for enhancing both the power and energy densities are proposed based on the predictions and experiments for the batteries.

Received 00th January 20xx,
Accepted 00th January 20xx
DOI: 10.1039/x0xx00000x

Introduction

Sodium ion batteries (SIBs), as a promising alternative to lithium ion batteries (LIBs), have received an extensive attention recently because sodium possesses excellent electrochemical properties similar to lithium in the same alkali group and abundant resources with the cost 40 times lower than lithium.¹⁻⁵ Various cathode materials including transition metal oxides (NaCoO₂ and Na_xMnO₂), phosphates (NaMPO₄ (M= Fe, Mn, Co, etc.)), and fluorides (NaMF₃ (M=Ni, Fe, Mn)) have been developed and proved to be comparable performance to lithium-ion batteries.⁶⁻¹⁰ However, the design of anode materials with high rate capability and capacity, superior reliability and safety, and long cycle life has always been a major scientific challenge,¹¹ which directly restricts comprehensive performance of the ion full batteries.

Considering the similarity of working mechanism between the two kinds of batteries, until now, following the design concepts for anode materials of LIBs, many ion diffusion-controlled anode materials for SIBs (Table S1, Supporting Information) have been developed including carbon materials such as graphite,¹² carbon fibers,¹³ and acetylene black,¹⁴ and

Na-alloy material consisting of Na₁₅Ge₄,¹⁵ Na₁₅Sn₄,¹⁶ Na₁₅Pb₄,¹⁷ Na₃P,¹⁸ and Na₃Sb,¹⁹ and even bifunctional hybrid materials made by incorporating alloy materials into graphene backbone.²⁰ Although these materials significantly improve the capacity of SIBs, they all have a common weakness—low rate capability—owing to slow ion diffusion in bulk host materials due to the deintercalation/intercalation process laboriously caused by smaller interlayer distance and huge volume expansion of electrode originating from alloying reaction. In fact, the above problems in SIBs are severer than LIBs as a sodium ion has larger radius (1.02 Å) and higher molar mass (23), requiring a layer spacing of at least 3.7 Å for reversible deintercalation/intercalation, which inevitably gives rise to poor diffusion rate in bulk electrode and considerable technical difficulty for designing such anode materials. Other emerging ion-based batteries such as potassium ion batteries (KIBs),²¹ calcium ion batteries (CaIBs),²² zinc ion batteries (ZIBs),²³ and aluminium ion batteries (AlIBs),²⁴ face similar challenges in the design of anode materials.

To overcome the challenges, one promising route for the design of anode materials is to use capacitive process-controlled materials instead of traditional ion diffusion-controlled materials. While enhancing the ion transportation in bulk electrodes, this approach would avoid various shortcomings such as volumetric expansion and severe interlayer width. Along this line, there have been several reports on the anode materials that operate to achieve high rate in pseudocapacitive mechanism for storage of sodium ions (Table S1, Supporting Information), including graphene-based nitrogen-doped carbon sandwich nanosheets,²⁵ hierarchical layered graphene composites,²⁶ and ferroelectric Sn₂P₂S₆ with

^a State Key Laboratory of Solidification Processing, School of Materials Science and Engineering, Northwestern Polytechnical University, Xi'an 710072, China

^b Department of Mechanical Engineering, University of Delaware, Newark DE 19716, United States

^c Department of Materials Science and Engineering, Department of Chemistry, University of North Texas, Denton, TX 76203, USA, E-mail: Zhenhai.xia@unt.edu

*Electronic Supplementary Information (ESI) available: [details of any supplementary information available should be included here]. See DOI: 10.1039/x0xx00000x

layered nanostructures with pseudocapacitive sodium storage.²⁷ Among them, heteroatom-doping technique has attracted more attention in improvement of the capacity and rate of carbon anode, particularly capacitive process-controlled carbon anode in SIBs. It has been demonstrated that heteroatom dopants (e.g., N, B, S, P, or F) can significantly enhance both capacity and rate capability of carbon-based SIBs (Table S2, Supporting Information).²⁸⁻³²

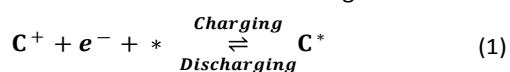
Despite the potential of heteroatom-doped carbon nanomaterials for ultrafast SIBs, trial-and-error approaches are still used to date for the development of SIBs. To rationally design effective anode materials for the ultrafast SIBs, it is necessary to correlate the doping structures to the capacity of carbon-based anode. Some work has been done by using the first-principles calculations to understand the energy storage mechanisms and to estimate charge storage ability of heteroatom-doped carbon electrodes.³³⁻³⁵ For the entire family of metal-free carbon-based electrodes, however, there is a lack of design principles or intrinsic descriptors that govern charge storage activities.

Herein, the graphene structures doped with p-block elements in the periodic table were used as anode materials of SIBs and KIBs for the sodium and potassium ions storage. The capacity C and rate capability P are correlated with the heteroatom-doping structures of carbon nanomaterials by an intrinsic descriptor that can be used for screening the best electrode materials. The predictions are consistent with the experimental results. The results reveal the transition from capacitive mechanism to phase reaction mechanism in the process of sodium and potassium ions storage, from which the design principles are established for enhancing both capacity and rate capability of carbon-based anode materials for SIBs and KIBs simultaneously. The results provide a theoretical base for searching for the desired carbon-based anode materials for ultrafast SIBs and KIBs.

Results

Mechanism and Origin of Heteroatom-doped Graphene for Na⁺ and K⁺ Storage

Active Sites for Na⁺ and K⁺ Storage in Heteroatom-doped Carbon. Graphene doped with p-block elements X (X=B, Si, N, P, Sb, O, S, F, Cl, Br, and I), as an anode, was modeled, as shown in Fig. 1a and Fig. S1(Supporting Information). The doping density of the models is 1.8 at% for zigzag graphene, 2.1 at% for graphene nanosheet, and 2.8 at% for armchair graphene model, which is similar to that in the experiments. Upon charging, sodium ions in neutral electrolyte (0.5 M Na₂SO₄) or potassium ions in alkaline electrolyte (6 M KOH) driven by external electric potential U are chemisorbed on the sites of the anode surface to combine electrons from external circuit through the reaction:



where * denotes the sites of doped graphene electrode, and C⁺ and C* are the dissociative sodium or potassium ions in electrolyte and those chemisorbed on the electrode,

respectively. The discharging process is the reversible reaction of Eq.1, in which chemisorbed sodium or potassium ions desorb from the anode surface.

To identify active sites for the storage of ions, the chemical adsorption energy ΔG_{C^*} of the ions at all possible sites of the doped graphene was calculated. The adsorption positions of sodium and potassium atoms on doped/pure graphene models, together with the adsorption energy, are shown in Figs. S2-S5 (Supporting Information). Unlike the protons that are directly absorbed on the carbon atoms in the capacitors,³⁶ sodium and potassium occupy the hollow positions of the graphene due to their relatively large size, as shown in the insets of Fig. 1b. The chemical adsorption energy ΔG_{C^*} distributes unevenly on different positions due to the edge and doping effects, as shown in Figs. S5 and S6 (Supporting Information). In the charging process, cations (Na⁺ or K⁺) may firstly adsorb on the sites with the lowest chemical adsorption energy ΔG_{C^*} (ΔG_{Na^*} and ΔG_{K^*}) due to its lowest energy barrier. This site serves as the starting point of the whole charging process. The ions will then deposit

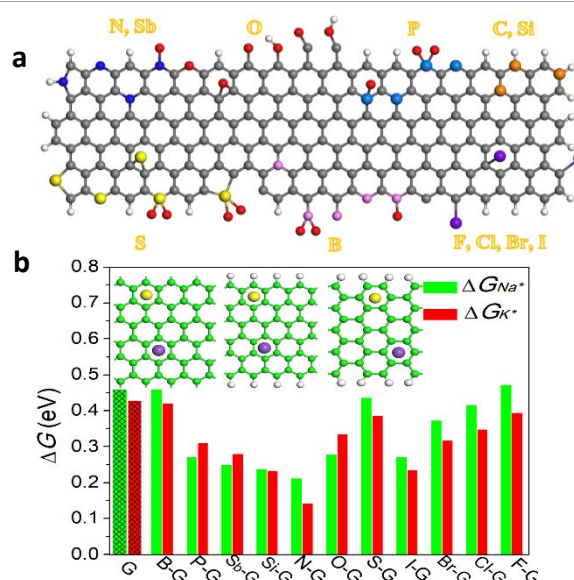


Fig. 1. **a.** Summary of the heteroatom doping modes: (top row, from left to right) pr-N(Sb), py-N(Sb), g-N(Sb), N(Sb)-O, py-O, C-O-C, C=O, C-OH, C-C=O, C-C-OH, P-3C-O, P-3C, P-2C-2O, P-2C, g-C(Si), z-C(Si) and a-C(Si); (bottom row, from left to right) th-S, py-S, S-O-S, S-2O, th-S-2O, B-3C, B-C-2O, B=C, B-2C, B-2C-O, z-(F, Cl, Br, and I), g-(F, Cl, Br, and I) and a-(F, Cl, Br, and I); Orange/grey, green, pink, light blue, yellow, red, purple, and white balls represent C(Si), N(Sb), B, P, S, O, F, Cl, Br, and I, and H atoms, respectively. **b.** Bar graph of computed minimum positive Gibbs free energy ΔG_{Na^*} and ΔG_{K^*} at $U=0$ and the insets represent the hollow sites adsorbing Na and K for different graphene structures (from left to right: inplane, zigzag-edged and armchair-edged graphene, and green, while, yellow and purple balls in these graphene represent C, H, Na and K, respectively).

on the positions with the second lowest adsorption energy, and, this process successively continues till all the positions are

occupied. After all the positions are filled, the ion could further deposit on the surface of the adsorbed ion layer.

Although all the positions could be occupied in the charging process, not all adsorbed ions can be released during discharging. Specifically, only those ions adsorbed at the sites with $\Delta G_{C^*} > 0$ can be released to electrolytes. Thus, according to the values of ΔG_{C^*} and ion deposition positions the sites can be divided into three categories: (i) irreversible adsorption sites ($\Delta G_{C^*} < 0$), (ii) reversible adsorption sites ($0 < \Delta G_{C^*} < \Delta G_T$), and (iii) stacking sites ($\Delta G_{C^*} > \Delta G_T$), where ΔG_T is the free energy of phase transition (atom stacking). For the irreversible adsorption sites, since the adsorption energy is negative ($\Delta G_{C^*} < 0$), ions can chemisorb on them spontaneously but cannot desorb in the discharging. Hence the ions on these sites are ineffective and have no contribution to the charge storage. In the case of the reversible charge storage sites with $\Delta G_{C^*} > 0$, the adsorbed ions (Na^+ or K^+) could be spontaneously released during the discharge. However, when $\Delta G_{C^*} > \Delta G_T$, nucleation and growth of bulk metal sodium or potassium phase could occur. This marks the transition from pseudocapacitive mechanism in supercapacitors to metal deposition mechanism existing in lithium-, sodium- and potassium-metal batteries.

Since only the sites with $\Delta G_{C^*} > 0$ are the active sites for charge storage, the minimum positive chemical adsorption $\Delta G_{C^*}^{\text{min}}$ is important and can be considered as an indicator of effective ion storage on heteroatom-doped carbon electrode surface. $\Delta G_{C^*}^{\text{min}}$ for pristine and doped graphene structures was calculated and shown in Fig. 1b.

Transition from Surface-Induced Pseudocapacitive Mechanism to Metal Battery Mechanism for Na^+/K^+ Storage. As mentioned above, ions will deposit successively on the active sites of the graphene, during which the energy for depositing atoms will be different due to the edge and doping effects as well as the interaction between the adsorbed ions and depositing ions. We have simulated the ion deposition (charging) process on pristine and doped graphene structures (Fig. 2a) and further calculated the chemical adsorption energy ΔG_{Na^*} for each site. Fig. 2b shows the dependence of adsorption energy ΔG_{Na^*} on the number of chemisorbed Na^+ (or the coverage θ) for all heteroatom-doped graphene substrates including pure graphene. At the beginning of the deposition, ΔG_{Na^*} increases almost linearly with increasing the number of the chemisorbed ions and then gradually reaches a plateau. Similar deposition features were also found in doped graphene electrode structures with defects, as shown in Fig. S8 (Supporting Information). The increased adsorption energy can be attributed to the increased lateral repulsive interaction resulting from more sodium ions adsorbed on surface. In addition, sodium ions adsorbed on anode surface gradually rearrange to form more regular monolayer with the increase of sodium ions adsorbed on substrate, as illustrated in Fig. 2a. Obviously, the topological structure of the monolayer is strongly affected by the topological structure of the graphene substrate.

After the monolayer is formed or even before the graphene surface is completely covered ($\theta = 100\%$), ions start to deposit on the top of the monolayer and the second deposition layer

merges, as shown in Fig. 2a. In this stage of ion deposition as observed in lithium-, sodium- and potassium-metal batteries, the adsorption energy ΔG_{Na^*} becomes constant after $\theta > 100\%$, as shown in Fig. 2b, corresponding to constant charging/discharging electric potential, as shown in Fig. 2c. Thus, from the adsorption energy and deposition coverage changes, it is clear that the charging involves an initial ion adsorption in capacitive mechanism, followed by the metal-multilayer formation in metal-battery mode.

For potassium ion (K^+) storage, almost the same mechanism was also demonstrated, as shown in Fig. 3. However, compared with sodium ions (Na^+), there are two key differences: i) higher

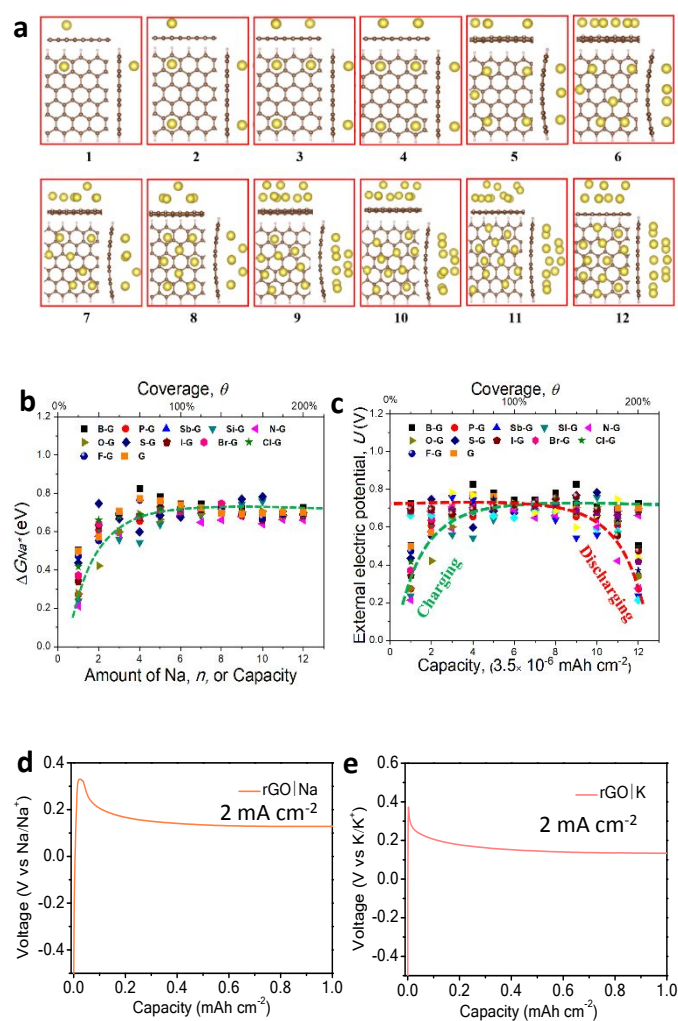


Fig. 2. **a.** Structural evolution upon sodium atoms deposition on z-C graphene model. The number from 1 to 12 refers to the number of ions deposited on the surface of the graphene. **b.** External electric potential U (vs. Na^+/Na) versus amount of Na chemisorbed on the optimal p-block elements doped graphene models (or Coverage, θ). **c.** External electric potential U (vs. Na^+/Na) versus capacity on the optimal p-block elements doped graphene models (or Coverage, θ) for charging and discharging process. **d.** Profiles of voltage vs. capacity for Na deposition on

rGO at 2 mA cm^{-2} . **e.** Profiles of voltage vs. capacity for K deposition on rGO at 2 mA cm^{-2} .

free energy of phase transition ΔG_T , which was also demonstrated by our electrochemical test and ii) more potassium deposition in the monolayer. As illustrated in Figs. 2a and 3a, for the same substrate with the same area, upon the 7-th sodium atom deposition on substrate, the phase transition occurs with the growth of the second sodium layer, while for potassium deposition, the second potassium layer does not start to grow until the 11-th potassium atom is chemisorbed. The difference is mainly ascribed to the stronger adsorption binding of graphene to potassium ions, and hence the doped graphene electrodes are capable of storing more potassium ions based on capacitive mechanism compared with sodium ions storage.

To experimentally demonstrate this transition mechanism predicted from the DFT calculation, Na and K ion batteries were made using Na and K plating/stripping on reduced graphene oxide (rGO) electrodes and charging experiment was performed (See details in methods). The results showed that the change of external electric potential U versus capacity C for both Na and K deposition consists of two parts, namely linear increase and plateau stability, as illustrated in Figs. 2d-e, which is in good agreement with our DFT predictions. The predicted trend of potential U versus capacity C is also in line with the capacitive characteristics, as shown in Fig. S7 (Supporting Information). In

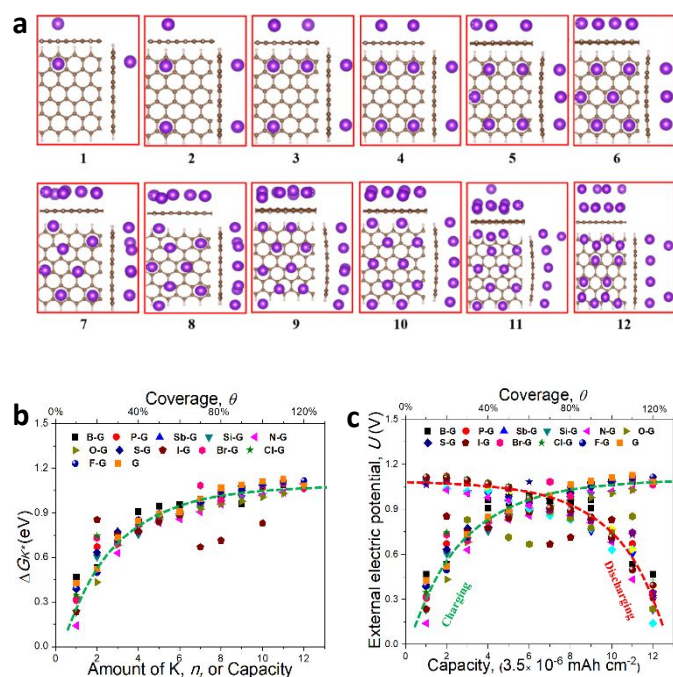


Fig. 3. **a.** Structural evolution upon potassium atoms deposition on z-C graphene model. The number from 1 to 12 refers to the number of ions deposited on the surface of the graphene. **b.** ΔG_{K^*} versus the amount of K chemisorbed on p-block elements doped graphene models (or Coverage, θ). **c.** External electric potential U (vs. K/K^+) versus the capacity of p-block elements

doped graphene models (or Coverage, θ) for charging and discharging processes.

In addition, negative electric potential U for charging in experiment originates from negative irreversible adsorption sites resulting from defects of rGO anode, as demonstrated in DFT calculation.

In Na-/K-metal batteries, one of the big issues is the inevitable growth of dendritic Na and K during cycling, which usually results in low Coulombic efficiencies, internal short circuits, unnecessary waste of Na and K metals, and even catastrophic cell failures. This would cut down the energy and power densities of full battery cells and hinder the commercialization.³⁷ We have further simulated the growth of K and Na bulk metals on the graphene surface. As observed in Figs. 4b-d, the metals grow along a certain direction of the graphene in the plane manner of layer by layer while the external electric potential still keeps stable (Fig. 4a). The orientation and topological structures of the bulk metals are very similar to the preferred growth of lithium ions on graphene substrate, as observed in the experiments. Specifically, as illustrated in Figs. 4c-d, the first two layers of potassium and sodium atoms in bulk potassium and sodium metal phase orientate in certain angle on graphene nanoribbons. Both K and Na atoms on the graphene distribute like those in (110) plane in a BCC structure. The K [111] and Na [111] directions are parallel to the zigzag edge of graphene (Figs. 4c-d). Interestingly, the (110) spacing of K (3.762 \AA) and Na (3.034 \AA) are approximately

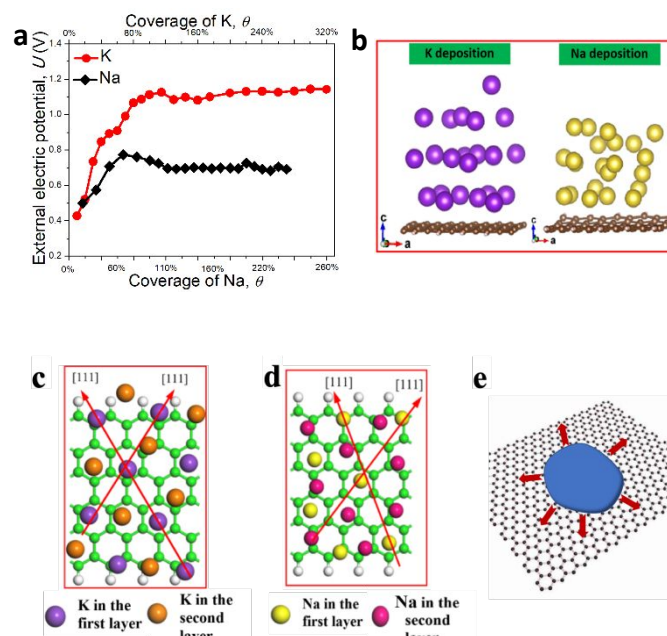


Fig. 4. **a.** The external electrical potentials versus coverage (θ) of Na and K chemisorbed on zigzag graphene models, **b.** Multilayered bulk phase structure of K and Na deposited on substrates. **c.** Distribution and orientation of the first two layers of potassium atoms on z-C model. **d.** Distribution and orientation of the first two layers of sodium atoms on z-C

model. **e.** Schematic of planner growth of sodium and potassium on the surface of graphene.

1.5 and 1.2 times the length of one carbon hexagon (2.478Å) along the graphene zigzag direction. This orientation and topological matches between the metal and substrate would indicate a preferential growth of metals on the substrate. In general, if lattice mismatch δ is 5%, the corresponding surfaces of two phases can be coherent. We have calculated the lattice mismatches of Na, K, and Li with the graphene substrates (Table S3) according to the formula of lattice mismatch,

$$\delta = \frac{a_s - n \times a_N}{a_N},$$

where a_s and a_N are the spacings of substrate and crystal nucleus atoms, respectively, and n represents the multiplier factor. The lattice mismatches with the graphene for K and Na are 1.82% and 2.44%, respectively. Such small lattice mismatches may lead to the epitaxial alignment between the planar K and Na and graphene. These simulation results indicate that graphene substrate can guide the preferentially planner growth of K and Na during the long-term and repeated electrodeposition process (Fig. 4e). While the rate and capacity could be significantly enhanced, this planner growth could inhibit dendrite development effectively in potassium- and sodium-batteries.³⁹ Although the above prediction has not been confirmed experimentally, lithium batteries did show a guided growth of planar Li layers, instead of random Li dendrites, on self-assembled reduced graphene³⁸. The graphene substrate still renders the planar Li feature after 100 cycles while there are severe dendritic Li grown onto the Cu foil. This experimental result demonstrates the long-term stability of the graphene-guided directional growth of the planar layers of Li, and possibly K and Na.

Design Principle of Heteroatom-doped Carbon-Based Pseudocapacitive Anode Materials

An effective strategy for rationally designing an anode material is to establish a direct correlation between the intrinsic descriptor of the material and its specific capacitance C or energy density E . In our previous work,^{36, 40} we showed that the active sites of the doped graphene structures was correlated with a descriptor: the intrinsic physical quantities of dopants, electronegativity E_X and electron affinity A_X by

$$\emptyset = \frac{E_X A_X}{E_C A_C} \quad (2)$$

where E_X and A_X are electronegativity and electron affinity of heteroatoms, respectively, and E_C and A_C are electronegativity and electron affinity of carbon, respectively. On the other hand, in the case of surface-dominated anodes uptaking and absorbing sodium and potassium ions during the electrochemistry process, our simulation results show that the minimum adsorption energy ΔG_C^{min} is important and related to the specific capacitance $C_{0/site}$ (unit, e V⁻¹) in the range of $\Delta G_C^{min} < eU < \Delta G_C^{max} = \Delta G_T$ by³⁶

$$C_{0/site} = \frac{\frac{1}{2} e^2 \left(\frac{eU - \Delta G_C^{min}}{\Delta G_C^{max} - \Delta G_C^{min}} \right)^2}{\frac{eU k_B T}{eU - \Delta G_C^{min}} \ln \left[\frac{1}{2} \left(1 + e^{\frac{eU - \Delta G_C^{min}}{k_B T}} \right) \right]} \quad (3)$$

where U is the external potential, e and k_B are the charge of an electron and Boltzmann constant, respectively, and ΔG_C^{min} , ΔG_C^{max} and ΔG_T are the minimum positive free energy, the maximum free energy and the free energy of phase transition (See details in Supplementary), respectively. According to Eq. 3, the specific capacitance increases sharply with reduction of ΔG_C^{min} , and this analytic result from Eq.3 is consistent with the DFT calculation, as shown in Fig. 5a.

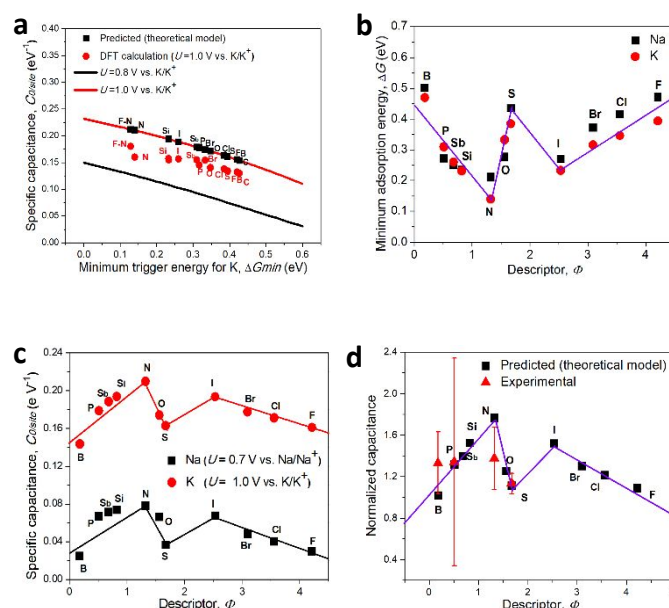


Fig. 5. **a.** The capacitance of unit charge storage site versus minimum Gibbs free energy at $U = 0.8$ and 1.0 V versus K/K^+ predicted according to the theoretical model and DFT calculation. **b.** The minimum Gibbs free energy of adsorption versus descriptor. **c.** The capacitance of unit charge storage site versus descriptor at potential U of 0.7 V and 1.0 V for Na and K, respectively. **d.** Measured specific capacitance from electrochemical ($U = 0.7$ V vs. Na/Na^+) and experimental ($U = 1.0$ V vs. K/K^+) measurements, normalized by undoped pure carbon-based electrode in alkaline (KOH) electrolyte under the same condition in the same experiment (Tables S6). The predicted specific capacitance according to theoretical models, normalized by undoped graphene, is also plotted against the descriptor.

We have correlated the minimum positive free energy ΔG_C^{min} and the specific capacitance with the descriptor. Since the phase transition energy ΔG_T is about 1 eV and 0.7 eV for both potassium and sodium ions adsorption, respectively, the potential U in Eq. 3 was set to 1V and 0.7V to calculate the specific capacitance for KIBs and SIBs. Fig. 5b, c shows the minimum positive free energy and the specific capacitance as a function of the descriptor \emptyset , respectively. Obviously, there are

dual volcano relationships with N-doping and I-doping at the peaks (Fig. 5c), which correspond to two minima of the curve in Fig. 5b. Therefore, N-doped graphene stands out among the p-block elements doped materials as the best anode materials.

To verify the volcano relationship predicted by the descriptor Φ , relevant experimental data were cited from the literature, as listed in Tables S6 and S7. To reliably compare the measured specific capacitances with our predictions, firstly, all the experimental data cited in this work were selected under the same conditions: the same alkaline electrolyte (KOH) and neutral electrolyte (Na₂SO₄). Secondly, all experimental data obtained were on the basis of capacitive charge storage mechanism, avoiding the contribution from other charge storage mechanism. Thirdly, two methods including theoretical model (equation (3)) and accumulation one by one by

$$C_{0/site} = \frac{1}{M} \sum_{i=1}^N \frac{e^2}{\Delta G_{C_i}^*} \quad (\Delta G_{C_i}^* < \Delta G_T)$$

according to DFT calculation were used to calculate predicted specific capacitance for more reliable comparison with experimental values. Finally, the specific surface area is accounted for in the calculations of specific capacitances (capacitance per unit area). The specific capacitances were then normalized by the specific capacitance of undoped graphene electrode, measured under the same conditions in the same experiments. Although morphology of the materials and dopant content could also affect the specific capacitances, since only graphene and some nanocarbon spheres were selected, their morphology and dopant content are similar and comparable. To further minimize the possible surface area/morphology/dopant content effects, we have averaged the data that were carefully selected from the literature.

Theoretical computing specific capacitance of the X-G were also normalized by that of undoped graphene, and made a comparison with the experimental data. Fig. 5d shows the normalized capacitances as a function of the descriptor for the X-G. Both DFT calculation and the experimental results show a volcano relationship with nitrogen sitting on its top, which agrees well with the predictions of theoretical model. Thus, the descriptor provides a theoretical tool to predict the energy storage capacity of the X-G, from which the best electrode materials could be selected.

The predictive power of the descriptor Φ mainly originates from the intrinsic physical meaning that correlates the properties to the structure of active sites, as mentioned in our previous study.³⁶ In terms of the definition of Pauling and Mulliken, the electric potential for an electrode μ depends on strongly its electronegativity, and can be expressed as $\mu \approx -\chi_M$, where χ_M is Pauling and Mulliken electronegativity. From the perspective of external circuit, increased electric potential results from accumulation of more and more electrons, which will lead to the relationship that $eU = \mu(N+1) - \mu(N)$ for per each added electron, where $\mu(N)$ and $\mu(N+1)$ denote the chemical potential of electrode (here, it is doping graphene) with N-electrons and (N+1)-electrons at ground state. Finally, at ground state, capacity can be derived to electronegativity, or our descriptor by

$$C_{0/site} = \frac{e^2}{\chi_M(N) - \chi_M(N+1)}$$

based the definition of capacitance. Consequently, the capacitance directly relies on the electronegativity. The dual-volcano-shaped relationship probably originates from the difference in doping sites. As shown in Fig. 1a and Table S4 (Supporting Information), the doping structures are quite different: on the left side of N, including N, dopants are embedded into the graphene lattice to form sp² chemical bonds with two and even three carbon atoms, but on the right side of N, most dopants can only attach on the edge of the graphene, or adsorb on the surface of graphene by grafting. Thus, the doping structures can be identified from the descriptor, which provide an insight into the charging storage mechanism.

Simultaneous Improvement of both Capacity and Rate by Dual element-Doping

According to the predictions of the above volcano relationship and charge storage origin, there is still a large room for us to

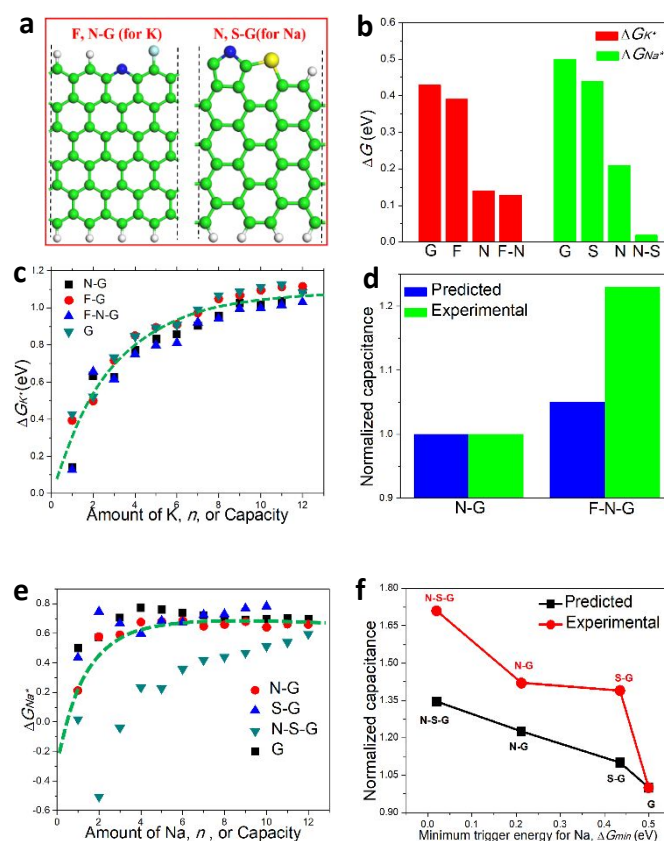


Fig. 6. a. the selected optimal models of F, N-codoped graphene for K storage and N, S-codoped graphene for Na storage among all possible 30 codoped models. b. the minimum Gibbs free energy ΔG_{min} for Na and K adsorption on corresponding mono- and multi-doped graphene models. c. the comparison between change of Gibbs free energy for F, N-codoped and mono-doped graphene models adsorbing K. d. the comparison between predicted capacitance and experimental data for K storage by normalization.[41] e. the comparison between the change of Gibbs free energy for N, S-codoped and mono-doped graphene

models adsorbing Na. **f.** the comparison between predicted capacitance and experimental data for Na storage by normalization.[42]

improve the capacitance towards the ideal charge storage capacity corresponding to zero charge storage energy barrier (Fig. 5b). Here, a strategy of co-doping is used to further increase the charge storage capacity. Since N is the best dopant among the p-orbital elements, it is selected to combine with the dopants S and F to form N, S and N, F co-doped graphene structures to store Na and K (Fig. 6a). $\Delta G_{Na^*}^{min}$ and $\Delta G_{K^*}^{min}$ were determined using the same method as the single-element doping (Fig. 6b). As expected, $\Delta G_{Na^*}^{min}$ and $\Delta G_{K^*}^{min}$ can be further reduced by co-doping, and the capacity of the anode in SIBs and KIBs can be pushed to its limitation (Figs. 6d-f). These predictions are consistent with the experimental results.⁴¹⁻⁴² The improved capacity can be attributed to the synergistic effect originating from the valance electron interactions between dopants.⁴³ Here, it deserves to note that predicted specific capacitance should be larger than that in the electrochemical experiment in general based on an ideal condition, but it is actually smaller. This discrepancy results from the fact that the ideal adsorption of monolayer metal ions was defined as the pseudocapacitive mechanism in our DFT calculation, but in the experiment, the electrode material surface may absorb more than one metal deposition layers. The deposition of the additional layers is possible, as predicted in Fig 4b, resulting in higher capacitive capacity. In addition, more ions may also be stored in the gaps between the reduced graphene layers but the mechanism should be classified into ion battery mechanism rather than pseudocapacitive mechanism. Anyway, both experimental results and predictions show that the capacitive performance of dual-element doping is indeed higher than that of single doping.

We have calculated the upper limit of the capacity of the doped graphene anode based on the charge storage mechanism. In fact, the charging process of the heteroatom-doped carbon anode in SIBs and KIBs is the process, in which several energy barriers must be overcome by applied external electric potential.³⁶ These include i) the thermodynamics energy barrier for adsorption (ie., ΔG_{Na^*} and ΔG_{K^*} in this study), ii) the energy barrier due to adsorbate interaction determined by intrinsic properties of adsorbates such as atomic radius, electronegativity, electron affinity and the charge carried by ions, etc., iii) the energy barrier originating from thermal motion being represented by $k_B T$, and iv) the phase transition energy barrier ΔG_T mainly relying on the adsorbed ion itself. Therefore, even if the adsorption energy barrier ΔG_{Na^*} (or ΔG_{K^*}) is reduced to zero by doping, other energy barriers cannot be eliminated, letting alone the existence of external resistance, as shown Figs. 6c-e. Thermodynamically, the zero adsorption energy barrier ΔG_{Na^*} (or ΔG_{K^*}) corresponds to the upper limit of $C_{0/site} = e/[U(1+\exp(-eU/k_B T))] \approx e/U$ for $eU \gg k_B T$. Therefore, the capacity depends only on electric potential for single site under zero energy barrier. The capacitance per unit charge storage site at the atomic level is different from the macroscopic capacitance that is independent of the amount of charge added

to the system and relies only on geometrical parameters of the system as well as dielectric constant.

In addition to the improved energy density (capacitance), the doping could further improve the power density (or rate). For a

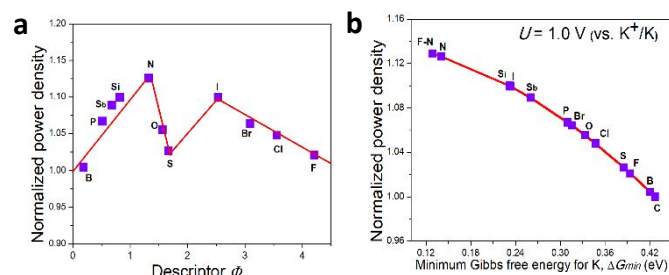


Fig. 7. **a.** Normalized power per unit site by undoped graphene versus descriptor Φ . **b.** Normalized power per unit site by undoped graphene versus minimum K adsorption energy $\Delta G_{K^*}^{min}$ at a given potential of $U = 1.0 \text{ V}$.

given external condition such as ohmic resistance, C^+ diffusion, conductivity and charging potential in a charging system, the rate of Na and K storage in surface-dominated anodes is mainly governed by the chemisorption rate of cations, and can be written as

$$P_{0/site} = k_0 \times \frac{eU k_B T \ln \left[\frac{1}{2} \left(1 + e^{-\frac{eU - \Delta G_{C^*}^{min}}{k_B T}} \right) \right] - \frac{1}{2} (\Delta G_{C^*}^{min} - eU)^2}{\Delta G_{C^*}^{max} - \Delta G_{C^*}^{min} + k_B T \left(e^{-\frac{\Delta G_{C^*}^{max} - eU}{k_B T}} + e^{-\frac{\Delta G_{C^*}^{min} - eU}{k_B T}} \right)} \quad (4)$$

where k_0 and k_B are the rate constant and the Boltzmann constant, respectively (See the details in Supplementary Information) According to Eq.4, the charging rate not only depends on the intrinsic factor such as the doping structures, but also relies on the extrinsic factors including charging potential U , electrolytes and pH value. For a given charging system, the doping generally enhances the power density as well as capacity, depending on the types of the dopants, as illustrated in Fig. 7 and Fig. S10 (Supporting Information). Overall, according to Eqs. 4 and S19 (Supporting Information), doping would reduce $\Delta G_{C^*}^{min}$, which would enhance both energy density and power density simultaneously for SIBs and KIBs based on pseudocapacitive mechanism.

Discussion

We have made DFT calculations to understand the origin of the X-G-based anode materials for surface-dominated SIBs and KIBs and discovered an intrinsic descriptor that well describes the energy storage capacity and rate of the anode materials. On the basis of the above results, both the energy and power densities are determined by intrinsic and extrinsic factors associated with active sites. As the adsorption occurs only on the active sites, the charge storage activity of the X-G is directly related to the unit activity of the active sites (intrinsic factor), while the population of exposed active sites for a given electrode mass in energy devices is the extrinsic factor, which is related to the

density of exposed active sites and the specific surface area (S_c). According to Eqs. 3 and 4, in addition to the intrinsic and extrinsic factors, environment factors (e.g., U and pH) also affect the proton adsorption of the electrodes. From above analysis, anode material design strategies can be established to achieve these predicted structures or functions by considering the intrinsic and extrinsic factors as well as the environmental factors. These strategies include as follows:

(i) Create highly-effective active sites. This anode material design strategy is to enhance the intrinsic activity of active centers (intrinsic factors). Doping using the p-block dopants with $0.5 < \phi < 1.5$ and $2.5 < \phi < 3.5$ and introducing more edges based on edge effect could significantly enhance the charge storage capacity. Co-doping, such as N, S and F, N co-doping, could further enhance the storage capacity due to the synergetic effect, as shown in Figs. 6a- b.

(ii) Build 3D nanoarchitectures to expose more active sites. This material design strategy is to populate more active sites on electrode surfaces (extrinsic factors). 3D porous carbon or nanoarchitecture electrodes could have a large specific-surface area to facilitate ion diffusion as well as increasing the number of exposed active sites. As illustrated in Fig. S9 (Supporting Information), the effective area could be increased by a factor of 2-10 by introducing carbon nanotube pillars, C_{60} and wrinkles on graphene surface. Of course, for a general battery, this will be an optimization problem that needs to balance the energy and power densities, especially for the development of lightweight and miniaturized electronic devices.

iii) Multilayer storage of Na and K ions on doped graphene surfaces. According to the analysis, the layers of Na and K atoms grow along (110) crystallographic plane of the Na and K crystals because of the fine in-plane lattice matching between Na and K and the graphene substrate, resulting in planar Na and K deposition. Thus, multilayer storage of Na and K ions on doped graphene surface is possible without introducing dendritic structures, which could significantly increase cycling performance and specific energy and power densities.

iv) Optimization of the width of interlayer gap. The wider interlayer gap is beneficial to transportation of sodium or potassium ions, further leading to high rate capability, namely power density. However, three-dimensional anode material, or bulk anode, cannot be used effectively. In addition, the width of interlayer gaps can result in the formation of diffusion layer along radial direction, which is ineffective in enhancing capacity. On the other hand, cations is not easy to transfer in the deeper interlayer gap, leading to higher diffusion overpotential. Overall, the ration of length to radius ($\chi=L/d$) for interlayer gap of anode materials should be optimized reasonably. Thus, an ideal doped method beyond dual doping can be used to reduce the energy barrier to zero, leading to the ideal capacitive performance for a given external condition. As mentioned above, for zero energy barrier, capacitance per unit site can be given by $C_{0/site} = e/[U(1+\exp(-eU/k_B T))] \approx e/U$ for $eU \gg k_B T$. Accordingly, for the same external electric potential U as shown in Table S4 (Supporting Information), this ideal capacitance will be $1.43 e V^{-1} \text{ site}^{-1}$ for sodium adsorption, which is almost 13

times larger than that of N, S co-doped graphene anode and $1 e V^{-1} \text{ site}^{-1}$ for potassium storage with a factor of 4.7 compared with that of F, N co-doped anode. Obviously, there is still a lot of room for the improvement of capacitance by heteroatom-doped strategy.

Conclusions

The charging/discharging processes on heteroatom-doped graphene anode materials in SIBs and KIBs were analyzed with the DFT methods. The Gibbs free energy of adsorption, the capacity, the energy and power densities were calculated to understand the origin of charge storage on the doped carbon surfaces. The results show that doping can significantly lower the Gibbs free energy of adsorption, and consequently enhance both energy and power densities. The co-doping can even further improve the charge storage capabilities due to the synergistic effect between the dopants. Introducing more graphene edges could also significantly enhance the charge storage capacity. A descriptor correlating charge storage capabilities with the doping structures was discovered, from which the optimal electrode structures could be predicted. In addition, graphene substrate can guide the preferential growth of K and Na during the long-term and repeated electrodeposition process, which could inhibit dendrite development effectively. Such a design principle provides a critical guidance for rational design of carbon-based electrodes for high-performance supercapacitors.

Methods

Simulation methods

The adsorption of sodium ions in neutral electrolyte and potassium ions in alkaline electrolyte during the charging process of SIBs and KIBs on various heteroatom-doped graphene surfaces were performed using the density functional theory (DFT) with spin polarization, as implemented in the Vienna ab-initio Simulation Package (VASP) code. The projector augmented wave (PAW) pseudo-potentials was used to describe nuclei-electron interactions, while the electronic exchange and correlation effects were modelled using the Perdew-Burke-Ernzerhof functional within the generalized gradient approximation (GGA). For plane wave basis set, a high kinetic energy cutoff of 400 eV was selected after testing several different cutoff energies. 10^{-5} eV was used as the convergence criterion of electronic structure iteration. For geometry optimization, convergence criterion for force of the system was set to be about 0.01 eV/Å. The K-points were set to be $4 \times 4 \times 1$ and $4 \times 1 \times 1$ for graphene sheet models and graphene nanoribbon models, respectively. The choice of the k point meshes and cutoff energy was able to ensure that energies converged to about 1 meV per atom.

Three different groups of graphene models were developed to explore the adsorption effects of electrolyte ions in the

charging process. The first group of graphene models are periodic in *x*- and *y*-directions, consisting of 48 carbon atoms. The second group of models are armchair graphene nanoribbons consisting of 36 carbon atoms and 8 hydrogen atoms used to saturate hanging bonds at the edges of graphene. The third group of models are zigzag graphene nanoribbons comprising 48 carbon atoms and 8 hydrogen atoms. Both armchair and zigzag nanoribbons were constructed as a three-dimensional periodic structure with vacuum layers around 14 Å and 18 Å in *y*- and *z*-directions, respectively, to avoid interaction between graphene slabs.

Experimental methods

The rGO substrates were prepared according to our previous work.³⁸ The Na metal and K metal used for asymmetric cells were prepared by rolling the Na/K into thin foils (0.5 mm in thickness) and then punching into 12 mm-diameter disks. CR2032 coin cells were employed for Na/K deposition testing. The electrolyte used for rGO|Na and rGO|K asymmetric cells are 1.0 M NaClO₄ in a mixed solvent of EC and DEC (1:1 in volume), and 1.0 M KPF₆ in a mixed solvent of EC and DEC (1:1 in volume), respectively. The Whatman glass microfiber are used as separators. All the cells were assembled in the argon-filled glovebox with the concentrations of moisture and oxygen below 0.1 ppm, and tested using a CT2001A cell test instrument (LAND Electronic Co, BT2013A, China) or an 88-channel battery tester (Arbin Instruments, BT2000, USA).

Conflicts of interest

There are no conflicts to declare.

Acknowledgements

This work is supported financially by National Science Foundation (1662288), the National Natural Science Foundation of China (51704243), the Fundamental Research Funds for the Central Universities (3102019ZD0402) and Innovation Foundation for Doctor Dissertation of Northwestern Polytechnical University (CX201943).

Notes and references

- M. D. Slater, D. Kim, E. Lee, C. S. Johnson, *Adv. Funct. Mater.*, 2013, **23**, 947.
- J. T. Xu, M. Wang, N. P. Wickramaratne, M. Jaroniec, S. X. Dou, L. M. Dai, *Adv. Mater.*, 2015, **27**, 2042.
- V. L. Chevrier, G. Ceder, *Journal of The Electrochemical Society*, 2011, **158**, A1011.
- P. Barpanda, G. Oyama, S. Nishimura, S. C. Chung, A. Yamada, *Nat. Commun.*, 2014, **5**, 4358.
- H. W. Lee, R. Y. Wang, M. Pasta, S. W. Lee, N. Liu, Y. Cui, *Nat. Commun.*, 2014, **5**, 5280.
- V. Palomares, P. Serras, I. Villaluenga, K. B. Hueso, J. Carretero-Gonzalez, T. Rojo, *Energy Environ. Sci.*, 2012, **5**, 5884.
- S. W. Kim, D. H. Seo, X. H. Ma, G. Ceder, K. Kang, *Adv. Energy Mater.*, 2012, **2**, 710.
- J. Xu, S. L. Chou, J. L. Wang, H. K. Liu, S. X. Dou, *ChemElectroChem*, 2014, **1**, 371.
- K. B. Hueso, M. Armand, T. Rojo, *Energy Environ. Sci.*, 2013, **6**, 734.
- P. Moreau, D. Guyomard, J. Gaubicher, F. Boucher, *Chem. Mater.*, 2010, **22**, 4126.
- W. L. Zhang, F. Zhang, F. W. Ming, H. N. Alshareef, *EnergyChem*, 2019, **1**, 100012.
- B. Jache, P. Adelhelm, *Angew. Chem., Int. Ed.*, 2014, **53**, 10169.
- Y. Wen, K. He, Y. J. Zhu, F. D. Han, Y. H. Xu, I. Matsuda, Y. Ishii, J. Cumings, C. S. Wang, *Nat. Commun.*, 2014, **5**, 4033.
- H. S. Hou, Y. C. Yang, Y. R. Zhu, M. J. Jing, C. C. Pan, L. B. Fang, W. X. Song, X. M. Yang, X. B. Ji, *Electrochimica Acta*, 2014, **146**, 328.
- S. Huang, C. Meng, M. Xiao, S. Ren, S. J. Wang, D. M. Han, Y. N. Li, Y. Z. Meng, *Sustainable Energy Fuels*, 2017, **1**, 1944.
- J. Park, J. W. Park, J. H. Han, S. W. Lee, K. Y. Lee, H. S. Ryu, K. W. Kim, G. X. Wang, J. H. Ahn, H. J. Ahn, *Mater. Res. Bull.*, 2014, **58**, 186.
- J. F. Qian, D. Qiao, X. P. Ai, Y. L. Cao, H. X. Yang, *Chem. Commun.*, 2012, **48**, 8931.
- L. Wang, X. M. He, J. J. Li, W. T. Sun, J. Gao, J. W. Guo, C. Y. Jiang, *Angew. Chem. Int. Ed.*, 2012, **51**, 9034.
- C. Marino, A. Debenedetti, B. Fraisse, F. Favier, L. Monconduit, *Electrochem. Commun.*, 2011, **13**, 346.
- J. Sun, H. W. Lee, M. Pasta, H. T. Yuan, G. Y. Zheng, Y. M. Sun, Y. Z. Li, Y. Cui, *Nat. Nanotechnol.*, 2015, **10**, 1038.
- L. W. Jiang, Y. X. Lu, C. L. Zhao, L. L. Liu, J. N. Zhang, Q. Q. Zhang, X. Shen, J. M. Zhao, X. Q. Yu, H. Li, X. J. Huang, Li. Q. Chen, Y. S. Hu, *Nature Energy*, 2019, **4**, 495.
- R. J. Gummow, G. Vamvounis, M. B. Kannan, Y. H. He, *Adv. Mater.*, 2018, **30**, 1801702.
- M. C. Lin, M. Gong, B. Lu, Y. Wu, D.-Y. Wang, M. Guan, M. Angell, C. Chen, J. Yang, B. J. Hwang, H. Dai, *Nature*, 2015, **520**, 324.
- C. Xu, Y. Chen, S. Shi, J. Li, F. Kang, D. Su, *Sci. Rep.*, 2015, **5**, 14120.
- D. D. Li, L. Zhang, H. B. Chen, J. Wang, L. X. Ding, S. Q. Wang, P. J. Ashman, H. H. Wang, *J. Mater. Chem. A*, 2016, **4**, 8630.
- Y. Yan, Y. X. Yin, Y. G. Guo, L. J. Wan, *Adv. Energy Mater.*, 2014, 1301584.
- S. Huang, C. Meng, M. Xiao, S. Ren, S. J. Wang, D. M. Han, Y. N. Li, Y. Z. Meng, *Small*, 2018, **14**, 1704367.
- Y. Wang, C. Y. Wang, Y. J. Wang, H. K. Liu, Z. G. Huang, *ACS Appl. Mater. Interfaces*, 2016, **8**, 18860.
- P. Z. Wang, B. Qiao, Y. C. Du, Y. F. Li, X. S. Zhou, Z. H. Dai, J. C. Bao, *J. Phys. Chem. C*, 2015, 119.
- Z. H. Wang, L. Qie, L. X. Yuan, W. X. Zhang, X. L. Hu, Y. H. Huang, *Carbon*, 2013, **55**, 328.
- H. S. Hou, L. Shao, Y. Zhang, G. Q. Zou, J. Chen, X. B. Ji, *Adv. Sci.*, 2017, **4**, 1600243.
- L. Qie, W. M. Chen, X. Q. Xiong, C. C. Hu, F. Zou, P. Hu, Y. H. Huang, *Adv. Sci.*, 2015, **2**, 1500195.
- C. Ling, F. Mizuno, *Phys. Chem. Chem. Phys.*, 2014, **16**, 10419.
- D. Datta, J. W. Li, V. B. Shenoy, *ACS Appl. Mater. Interfaces*, 2014, **6**, 1788.
- Y. Y. Liu, V. I. Artyukhov, M. J. Liu, A. R. Harutyunyan, B. I. Yakobson, *J. Phys. Chem. Lett.*, 2013, **4**, 1737.
- Y. Gao, J. Zhang, X. Luo, Y. Wan, Z. Zhao, X. Han, Z. H. Xia, *Nano Energy*, 2020, **72**, 104666.
- V. Palomares, P. Serras, I. Villaluenga, K. B. Hueso, J. Carretero-Gonzalez, T. Rojo, *Energy Environ. Sci.*, 2012, **5**, 5884.
- N. Li, K. Zhang, K. Xie, W. F. Wei, Y. Gao, M. H. Bai, Y. L. Gao, Q. Hou, C. Shen, Z. H. Xia, B. Q. Wei, *Adv. Mater.*, 2019, 1907079.
- D. C. Lin, Y. Liu, Z. Liang, H. W. Lee, J. Sun, H. T. Wang, K. Yan, J. Xie, Y. Cui, *Nat. Nanotechnol.*, 2016, **10**, 1038.

ARTICLE

Journal Name

- 40 Z. H. Zhao, M. T. Li, L. P. Zhang, L. M. Dai, Z. H. Xia, *Adv. Mater.*, 2015, **27**, 6834.
- 41 J. S. Zhou, J. Lian, L. Hou, J. C. Zhang, H. Y. Gou, M. R. Xia, Y. F. Zhao, T. A. Strobel, L. Tao, F. M. Gao, *Nat. Commun.*, 2015, **6**, 8503.
- 42 K. Gopalsamy, J. Balamurugan, T. D. Thanh, N. H. Kim, J. H. Lee, *Chemical Engineering Journal*, 2017, **312**, 180.
- 43 S. Bag, B. Mondal, A. K. Das, C. R. Raj, *Electrochimica Acta*, 2015, **163**, 16.